International Journal of Heat and Mass Transfer 52 (2009) 4135–4150

Contents lists available at ScienceDirect

International Journal of Heat and Mass Transfer

journal homepage: www.elsevier.com/locate/ijhmt

Finite element simulation of natural convection within porous trapezoidal enclosures for various inclination angles: Effect of various wall heating

Tanmay Basak [a], S. Roy [b,*], Sandeep Kumar Singh [b], I. Pop [c,*]

[a] Department of Chemical Engineering, Indian Institute of Technology Madras, Chennai 600 036, India
[b] Department of Mathematics, Indian Institute of Technology Madras, Chennai 600 036, India
[c] Faculty of Mathematics, University of Cluj, R-3400 Cluj, CP 253, Romania

ARTICLE INFO

Article history:
Received 1 April 2009
Accepted 28 April 2009
Available online 6 June 2009

Keywords:
Penalty finite element method
Natural convection
Porous medium
Trapezoidal cavity
Various angles
Linear heating

ABSTRACT

The phenomena of natural convection within a trapezoidal enclosure filled with porous matrix for linearly heated vertical wall(s) with various inclination angles φ has been studied numerically. A penalty finite element analysis with bi-quadratic elements is used for solving the Navier–Stokes and energy balance equations. Wide range of parameters such as Rayleigh number, $Ra(10^3 \leqslant Ra \leqslant 10^6)$, Prandtl number, $Pr(0.026 \leqslant Pr \leqslant 1000)$ and Darcy number, $Da(10^{-5} \leqslant Da \leqslant 10^{-3})$ have been used. Numerical results are presented in terms of streamlines, isotherms and Nusselt numbers. It has been found that secondary and tertiary circulations appear at the bottom half of the cavity for $\varphi = 30°$ and $\varphi = 0°$ with $Pr = 0.026$ and 0.7, $Da = 10^{-3}$ and $Ra = 10^6$ for linearly heated side walls. On the other hand, for linearly heated left wall and cold right wall, multiple circulations occur near the top portion of the cavity. For linearly heated side wall, the local Nusselt number (Nu_b) shows sinusoidal behavior with distance at high Darcy number for all tilt angles whereas increasing trend in Nu_s is observed in the upper half of the side wall for all tilt angles. For linearly heated left wall with cold right wall, increasing trend in Nu_b is observed irrespective to Da and Pr and Nu_b is even larger for higher Da. Increasing trend is also observed in Nu_t for all tilt angles for linearly heated left wall. Due to discontinuity in right corner, Nu_r first decreases and thereafter that increases for $Y \geqslant 0.2$. The average Nusselt number remains constant up to $Ra = 10^6$ at low Da for $Pr = 0.026$ whereas for $Pr = 1000$ and high Ra, that starts to decrease for bottom wall whereas that starts to increase for side walls due to convection dominant effect at high Da. In general, the average Nusselt number increases with the increase of Da and Ra for higher Da.

1. Introduction

Natural convection in closed cavities has occupied the center stage in many fundamental heat transfer analysis and has attracted many researchers' interest [1–11]. Processes involving natural convection in enclosures are important for rectangular and non-rectangular enclosures. However, the number of studies on natural convection in porous non-rectangular geometries is very limited. In this context, buoyancy driven phenomena in porous media are actively under investigation. Natural convection flows are highly non-trivial as the process depends on several parameters among which the geometry concerned and thermophysical characteristics of the fluid are the most important. Also, various applications depend on the product specification, shape of the container and heating characteristics. Numerical modeling can offer a way to reduce expensive experimental costs.

A good amount of the literature is available on the convection patterns in enclosures filled with porous media (Bejan and Poulikakos [12], Nield and Bejan [13], Ingham and Pop [14] and Al-Amiri [15]). Natural convection in an enclosure filled with two layers of porous media are investigated numerically by Merrikh and Mohamad [16]. Constant heat flux is imposed on the left vertical wall and the right wall is assumed to be at a low temperature. The focus of the work is on the validity of the Darcy model. Chen et al. [17] considered Darcy–Brinkman–Forchheimer extended model to examine free convection inside a porous cavity. This model has been initially introduced by Brinkman [18] in order to account for the transition from Darcy flow to highly viscous flow, in the limit of high permeability. Darcy–Forchheimer model is based on the effect of inertia and viscous forces in the porous media. This model was used by Poulikakos and Bejan [19] and Lauriat and Prasad [20] in order to investigate the natural convection in a vertical enclosure filled with a porous medium. The extended Darcy–Forchheimer model was also used to describe resistance to flow through the porous baffles by Miranda and Anand [21]. Al-Amiri et al. [22] investigated the wall heat conduction effect on the natural-convection heat transfer within a two-dimensional

* Corresponding authors.
E-mail addresses: tanmay@iitm.ac.in (T. Basak), sjroy@iitm.ac.in (S. Roy), san2007iit@gmail.com (S.K. Singh), pop.ioan@yahoo.co.uk (I. Pop).

0017-9310/$ - see front matter © 2009 Elsevier Ltd. All rights reserved.
doi:10.1016/j.ijheatmasstransfer.2009.04.016

Nomenclature

Da	Darcy number
g	acceleration due to gravity (m s^{-2})
k	thermal conductivity (W m^{-1} K^{-1})
H	height of the trapezoidal cavity (m)
Nu	local Nusselt number
p	pressure (Pa)
P	dimensionless pressure
Pr	Prandtl number
Ra	Rayleigh number
T	temperature (K)
T_h	temperature of hot bottom wall (K)
T_c	temperature of cold inclined wall (K)
u	x component of velocity
U	x component of dimensionless velocity
v	y component of velocity
V	y component of dimensionless velocity
X	dimensionless distance along x-coordinate
Y	dimensionless distance along y-coordinate

Greek symbols

α	thermal diffusivity (m^2 s^{-1})
β	volume expansion coefficient (K^{-1})
γ	penalty parameter
φ	angle of inclination
θ	dimensionless temperature
ν	kinematic viscosity (m^2 s^{-1})
ρ	density (kg m^{-3})
Φ	basis functions
ψ	streamfunction

Subscripts

b	bottom wall
l	left wall
r	right wall
s	side wall

cavity, which is filled with a fluid-saturated porous medium and their study was based on Forchheimer–Brinkman-extended Darcy model.

There are extensive studies available in the literature for natural convection in various rectangular porous cavities [23–26]. Varol et al. [24] have investigated numerically the steady natural convection flow through a fluid-saturated porous medium in a rectangular enclosure with a sinusoidal varying temperature profile on the bottom wall. They found that the heat transfer rate increases with increasing of amplitude of the sinusoidal temperature function and decreases with increasing aspect ratio. Multiple cells are observed in the cavity for all values of the parameters considered. Kim et al. [25] investigated numerically steady-state buoyant convection in a rectangular cavity, partially filled with a fluid-saturated porous medium with spatially uniform internal heat generation. Chang and Yang [26] analyzed numerically the transient flow field and heat transfer behavior of cold water in a rectangular enclosure filled with a porous medium. This result shows that as time increases, the heat transfer rate on the high-temperature surface decreases and that on the low-temperature surface increases.

Recent literatures also studied various complex situations in porous medium [27–33]. Waite and Amin [27] studied heat transfer and fluid flow mechanisms of two-phase fluid in porous enclosure with heated side walls. Kiwan and Alzahrany [28] have studied the steady-state, laminar, axisymmetric, natural convection heat transfer in the annulus between two concentric vertical cylinders using porous inserts. A finite volume method is used to solve numerically the sets of governing equations. Natural convection in an isosceles triangular enclosure filled with a porous matrix has been studied numerically with finite element method by Basak et al. [29]. A numerical investigation of natural convection heat transfer within a two-dimensional, horizontal annulus that is partially filled with a fluid-saturated porous medium has been carried out by Khanafer et al. [30]. Bera et al. [31] studied double-diffusive natural convective flow within a rectangular enclosure for an anisotropic porous medium using a non-Darcy extension. The results indicate that permeability orientation angle has a significant effect on the flow rate and, consequently, on the heat and mass transfer. Slimi et al. [32] investigated numerically coupled fluid flow and heat transfer by transient natural convection and thermal radiation in a vertical channel opened at both ends and filled with a fluid-saturated porous medium. Marcondes et al. [33] analyzed the effect of variable porosity on the heat transfer by natural convection in a cavity filled with porous medium. The hydrodynamic field in the porous medium is modeled based on the general model obtained by Brinkman and Forchheimer terms.

A few investigations on natural convection within trapezoidal enclosures have been carried out by earlier researchers [34–38]. Varol et al. [34] studied buoyancy-driven flow and heat transfer in an inclined trapezoidal enclosure filled with a fluid-saturated porous medium heated and cooled from inclined side walls. Their results show that inclination angle of the trapezoidal enclosure is more influential on heat transfer and flow strength than the influence due to the side wall inclination angle. Peric [35] studied natural convection in a trapezoidal cavities using control volume method and observed the convergence of results for grid independent solutions. Kuyper and Hoogendoorn [36] investigated laminar natural convection flow in trapezoidal enclosures to study the influence of the inclination angle on the flow and also the dependence of the average Nusselt number on the Rayleigh number. Thermosolutal heat transfer within trapezoidal cavity heated at the bottom and cooled at the inclined top part was investigated by Boussaid et al. [37]. The convective heat transport equation was solved by Alternating Direction Implicit (ADI) method combined with a fourth-order compact Hermitian method. Baytas and Pop [38] have studied natural convection on trapezoidal porous enclosure. Although a few studies of convection heating pattern within trapezoidal containers appear in the literature, no attempt has been made for the detailed flow and thermal analysis for trapezoidal porous enclosures with various inclination angles (as seen in Fig. 1a–c) in presence of various realistic thermal boundary conditions on side walls. The overall assessment of heat transfer rate via local and average Nusselt numbers at various walls of porous containers is important and detailed analysis has been carried out in this work. As a step towards the eventual development on natural convection flows within closed enclosures, it is interesting to pursue for a complete understanding of heat transfer rates for many engineering applications such as cooling of computer systems and other electronic equipments.

The present study deals with the natural convection within porous trapezoidal enclosures where the bottom wall is uniformly heated and vertical wall(s) are linearly heated or cooled whereas the top wall is well insulated. The effect of geometry has been illustrated for various angle of the side wall varying within 0–90°. In the current study, Galerkin finite element method with penalty parameter has been used to solve the nonlinear coupled partial

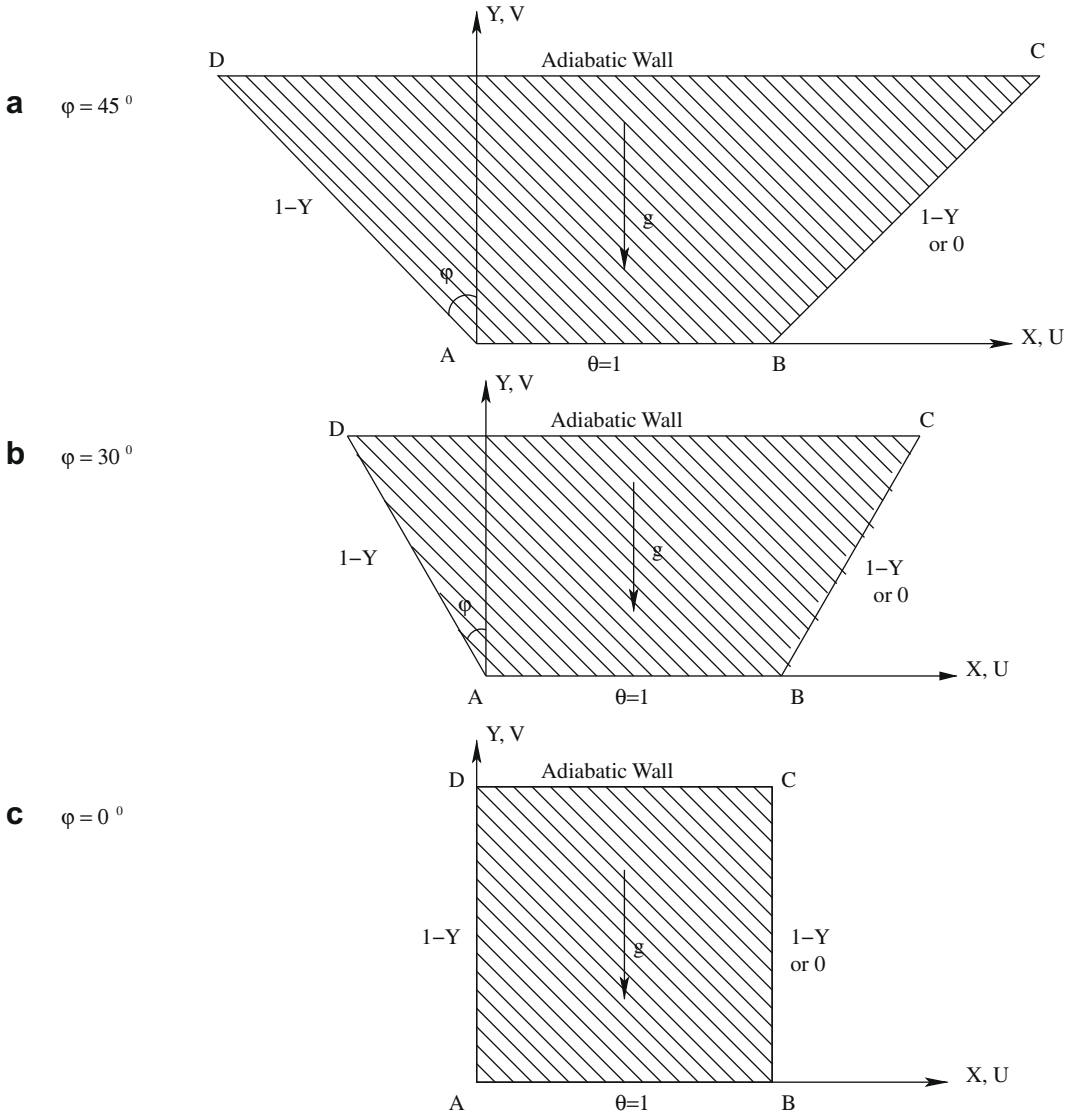

Fig. 1. Schematic diagram of the physical system for (a) $\varphi = 45°$, (b) $\varphi = 30°$ and (c) $\varphi = 0°$.

differential equations governing flow and temperature fields for both uniform and sinusoidally varying temperature distribution prescribed at side walls. Non-orthogonal grid generation has been done with iso-parametric mapping [39,40]. The momentum transfer in the porous medium is based on the Darcy–Forchheimer model with inertia term being neglected. Numerical results are obtained to display the circulations and temperature distributions within the trapezoidal enclosure and the heat transfer rate for both the walls in terms of local and average Nusselt numbers.

2. Mathematical formulation

Let us consider a trapezoidal cavity, filled with a porous medium, with the vertical walls inclined at an angle $\varphi = 45°$, 30° and 0° with y-axis as seen in Fig. 1(a)–(c), respectively. The velocity boundary conditions are considered as no-slip on solid boundaries. The liquid material is considered as incompressible, Newtonian and the flow is assumed to be laminar. For the treatment of the buoyancy term in the momentum equation, Boussinesq approximation is employed for equation of the vertical component of velocity to account for the variations of density as a function of temperature, and to couple in this way the temperature field to the flow field. Further, it is assumed that the temperature of the fluid phase is equal to the temperature of the solid phase everywhere in the porous body and local thermal equilibrium (LTE) is applicable in the present investigation [13]. Also, a velocity square term could be incorporated in the momentum equations to model the inertia effect which is more important for non-Darcy effect on the convective boundary layer flow over the surface of a body embedded in a high porosity media. However, this term has been neglected in the present study because this study involves the natural convection flow in a cavity filled with a porous medium. Under these assumptions and following the earlier work [41] with the Forchheimer's inertia term being neglected, the governing equations for steady two-dimensional natural convection flow in the porous cavity using conservation of mass, momentum and energy in dimensionless form can be written as:

$$\frac{\partial U}{\partial X} + \frac{\partial V}{\partial Y} = 0, \tag{1}$$

$$U\frac{\partial U}{\partial X} + V\frac{\partial U}{\partial Y} = -\frac{\partial P}{\partial X} + Pr\left(\frac{\partial^2 U}{\partial X^2} + \frac{\partial^2 U}{\partial Y^2}\right) - \frac{Pr}{Da}U, \tag{2}$$

$$U\frac{\partial V}{\partial X}+V\frac{\partial V}{\partial Y}=-\frac{\partial P}{\partial Y}+Pr\left(\frac{\partial^2 V}{\partial X^2}+\frac{\partial^2 V}{\partial Y^2}\right)-\frac{Pr}{Da}V+RaPr\theta, \tag{3}$$

$$U\frac{\partial \theta}{\partial X}+V\frac{\partial \theta}{\partial Y}=\frac{\partial^2 \theta}{\partial X^2}+\frac{\partial^2 \theta}{\partial Y^2}, \tag{4}$$

where

$$X=\frac{x}{H},\quad Y=\frac{y}{H},\quad U=\frac{uH}{\alpha},\quad V=\frac{vH}{\alpha},$$
$$P=\frac{pH^2}{\rho\alpha^2},\quad \theta=\frac{T-T_c}{T_h-T_c},\quad Pr=\frac{v}{\alpha},\quad Ra=\frac{g\beta(T_h-T_c)L^3}{v\alpha}, \tag{5}$$

with following boundary conditions:

$$\begin{aligned}
&U=0,\ V=0,\ \theta=1\ \ \forall Y=0,\ 0\leqslant X\leqslant 1,\\
&U=0,\ V=0,\ \theta=1-Y\ \ \forall X\cos(\varphi)+Y\sin(\varphi)=0,\ 0\leqslant Y\leqslant 1,\\
&U=0,\ V=0,\ \theta=1-Y \text{ or } 0\ \ \forall X\cos(\varphi)-Y\sin(\varphi)=\cos(\varphi),\ 0\leqslant Y\leqslant 1,\\
&U=0,\ V=0,\ \frac{\partial\theta}{\partial Y}=0\ \ \forall Y=1,\ -\tan(\varphi)\leqslant X\leqslant 1+\tan(\varphi).
\end{aligned} \tag{6}$$

3. Solution procedure

The momentum and energy balance equations [Eqs. (2)–(4)] are solved using the Galerkin finite element method. The continuity equation [Eq. (1)] will be used as a constraint due to mass conservation and this constraint may be used to obtain the pressure distribution. In order to solve Eqs. (2) and (3), we use the penalty finite element method where the pressure P is eliminated by a penalty parameter γ and the incompressibility criteria given by Eq. (1) results in

$$P=-\gamma\left(\frac{\partial U}{\partial X}+\frac{\partial V}{\partial Y}\right). \tag{7}$$

The continuity equation [Eq. (1)] is automatically satisfied for large values of γ. Typical values of γ that yield consistent solutions are 10^7. Using Eq. (7), the momentum balance equations [Eqs. (2) and (3)] reduce to

$$U\frac{\partial U}{\partial X}+V\frac{\partial U}{\partial Y}=\gamma\frac{\partial}{\partial X}\left(\frac{\partial U}{\partial X}+\frac{\partial V}{\partial Y}\right)+Pr\left(\frac{\partial^2 U}{\partial X^2}+\frac{\partial^2 U}{\partial Y^2}\right)-\frac{Pr}{Da}U, \tag{8}$$

and

$$U\frac{\partial V}{\partial X}+V\frac{\partial V}{\partial Y}=\gamma\frac{\partial}{\partial Y}\left(\frac{\partial U}{\partial X}+\frac{\partial V}{\partial Y}\right)+Pr\left(\frac{\partial^2 V}{\partial X^2}+\frac{\partial^2 V}{\partial Y^2}\right)-\frac{Pr}{Da}V+Ra\,Pr\,\theta. \tag{9}$$

The system of equations [Eqs. (4), (8) and (9)] with boundary conditions [Eq. (6)] are solved using Galerkin finite element method [39]. Since the solution procedure is explained in an earlier work [23], the detailed description is not included in this paper. The numerical solutions are obtained in terms of the velocity components (U,V) and streamfunction (ψ) is evaluated using the relationship between the streamfunction (ψ) and the velocity components [42], where the streamfunction (ψ) is defined in the usual way as $U=\frac{\partial\psi}{\partial Y}$ and $V=-\frac{\partial\psi}{\partial X}$. It may be noted that, the positive sign of ψ denotes anti-clockwise circulation and the clockwise circulation is represented by the negative sign of ψ. The no-slip condition is valid at all boundaries as there is no cross flow, hence $\psi=0$ is used for the boundaries. For steady flows, streamlines are equivalent to the paths followed by the individual particles in the fluid.

The heat transfer coefficient in terms of the local Nusselt number (Nu) is defined by

$$Nu=-\frac{\partial\theta}{\partial n}, \tag{10}$$

where n denotes the normal direction on a plane. The local Nusselt numbers at bottom wall (Nu_b), left wall (Nu_l) and right wall (Nu_r) are defined as

$$Nu_b=\sum_{i=1}^{9}\theta_i\frac{\partial\Phi_i}{\partial Y}, \tag{11}$$

$$Nu_l=\sum_{i=1}^{9}\theta_i\left(\cos\varphi\frac{\partial\Phi_i}{\partial X}+\sin\varphi\frac{\partial\Phi_i}{\partial Y}\right), \tag{12}$$

and

$$Nu_r=\sum_{i=1}^{9}\theta_i\left(-\cos\varphi\frac{\partial\Phi_i}{\partial X}+\sin\varphi\frac{\partial\Phi_i}{\partial Y}\right). \tag{13}$$

The average Nusselt numbers at the bottom, left and right walls are

$$\overline{Nu_b}=\frac{\int_0^1 Nu_b\,dX}{X|_0^1}=\int_0^1 Nu_b\,dX, \tag{14}$$

$$\overline{Nu_l}=cos\varphi\int_0^{\frac{1}{\cos\varphi}}Nu_l\,ds_1, \tag{15}$$

and

$$\overline{Nu_r}=cos\varphi\int_0^{\frac{1}{\cos\varphi}}Nu_r\,ds_2, \tag{16}$$

where ds_1, ds_2 are the small elemental length along the left and right walls, respectively.

4. Results and discussion

4.1. Numerical tests

The computational domain consists of 20×20 bi-quadratic elements which correspond to 41×41 grid points in Cartesian co-ordinate system and grid generation with iso-parametric mapping has been discussed in earlier work [43]. The bi-quadratic elements with lesser number of nodes smoothly capture the non-linear variations of the field variables which are in contrast with finite difference solution available in the literature [38]. Numerical solutions are obtained for various values of $Ra(10^3-10^6)$, $Pr(0.026-\ 1000)$ and $Da(10^{-5}-10^{-3})$ with uniformly heated bottom wall in presence of either linearly heated side walls or linear heated left wall with cooled right wall in presence of adiabatic top wall. It may be noted that the jump discontinuity in Dirichlet type of wall boundary conditions at the right corner point (see Fig. 1) corresponds to computational singularity. In particular, the singularity at the right corner of the bottom wall needs special attention.

To ensure the convergence of the numerical solution to the exact solution, the grid sizes have been optimized and simulation results are found to be independent of grid size. The grid size dependent effect upon the Nusselt numbers (local and average) due to temperature discontinuity at the corner point tends to increase as the mesh spacing at the corner is reduced. One of the ways for handling the problem is assuming the average temperature of the two walls at the corner and keeping the adjacent grid-nodes at the respective wall temperatures. Alternatively, based on earlier work by Ganzarolli and Milanez [44], once any corner formed by the intersection of two differentially heated boundary walls is assumed at the average temperature of the adjacent walls, the optimal grid size obtained for each configuration

corresponds to the mesh spacing over which further grid refinements lead to grid invariant results in both heat transfer rates and flow fields.

In the current investigation, Gaussian quadrature based finite element method provides the smooth solutions at the interior domain including the corner regions as evaluation of residual depends on interior Gauss points and thus the effect of corner nodes is less pronounced in the final solution. The present finite element approach offers special advantage on evaluation of local Nusselt number at the bottom and side walls as the element basis functions are used to evaluate the heat flux.

In order to assess the accuracy of the numerical procedure, computations are carried out on 20×20 bi-quadratic elements for a square domain ($\varphi = 0^\circ$) filled with air ($Pr = 0.71$) subjected to hot left wall and cold right wall in presence of insulated horizontal walls at $Ra = 10^5$ and the results are in well agreement with previous work [45]. It is found that the average Nusselt number ($\overline{Nu}$) based on current work is 4.5–4.6 whereas $\overline{Nu} = 4.52$ was obtained in the previous work [45].

4.2. Isotherms and streamlines: linearly heated side walls

Figs. 2–6 illustrate the isotherms and streamlines for various $Ra = 10^3$–10^6, $Da = 10^{-5}$–10^{-3} with $Pr = 0.026$–1000 in presence of uniformly heated bottom wall and linearly heated side walls. As expected due to linearly heated vertical walls and uniformly heated bottom wall, fluid rise up from the middle portion of the bottom wall and flow down along the two vertical walls forming two symmetric rolls with clockwise and anticlockwise rotations inside the cavity. Results indicate that the fluid circulations and isotherms are strongly dependent on Darcy number.

Fig. 2 displays the temperature and streamfunction contours for $Da = 10^{-5}$ and $Ra = 10^6$ with $Pr = 0.026$. In this case, intensity of the flow is very weak as observed from streamfunction contours. Consequently, the temperature contours are smooth and monotonic illustrating that heat transfer is primarily due to conduction. Isotherms with $\theta = 0.1$–0.7 occur symmetrically near the side walls of the enclosure for $\varphi = 45^\circ$ (Fig. 2a). The other isotherms with $\theta \geqslant 0.8$ are smooth curves symmetric with respect to vertical symmetric line at the center. The maximum value of streamfunction is 0.21. But, for $\varphi = 30^\circ$, the isotherms with $\theta = 0.1$–0.6 occur symmetrically near the side walls of the enclosure (Fig. 2b) whereas $\theta \geqslant 0.7$ are smooth curves symmetric with respect to vertical symmetric line. The maximum value of streamfunction is found to be 0.185. For square cavity ($\varphi = 0^\circ$), $\theta = 0.1$–0.3 is symmetric along the side walls and $\theta \geqslant 0.4$ are smooth curves symmetric with respect to the vertical symmetric line and the maximum value of streamfunction is 0.082 (Fig. 2c). It is observed that the intensity of circulation increases with the angle and larger temperature gradient is observed near the side walls with the increase in φ.

Fig. 3 shows the temperature and streamfunction contours for $Da = 10^{-4}$ and $Ra = 10^6$ with $Pr = 0.026$. The convection starts to play a dominant role and the isotherms are gradually pushed towards the side walls. It is observed that isotherms with $\theta \leqslant 0.8$ are pushed towards the side walls whereas temperature contours with $\theta \geqslant 0.9$ occur symmetrically for $\varphi = 45^\circ$. The maximum value of streamfunction is found to be 2.3 (see Fig. 3a). For $\varphi = 30^\circ$, the isotherms with $\theta \leqslant 0.8$ are shifted towards the side walls and $\theta \geqslant 0.9$ are continuous curves (Fig. 3b). It may be noted that the maximum value of streamfunction is 2.35. For square cavity, the isotherms with $\theta \leqslant 0.5$ are pushed towards the side walls whereas $\theta \geqslant 0.6$ contours occur symmetrically with respect to the vertical symmetric line and the maximum value of streamfunction is 1.85 (Fig. 3c).

As Da increases to 10^{-3}, the strength of the convection increases and the critical Rayleigh number for the conduction dominant mode is found as $Ra = 6 \times 10^4$ for all φ's. It may be noted that conduction is dominant below the critical Ra and above the critical Ra, the convection becomes dominant mode of heat transfer. At the onset of convection, the isotherms get distorted and move towards the side walls. Note that, the critical value of Ra has been obtained from asymptotes of average Nusselt number vs. Rayleigh number plot.

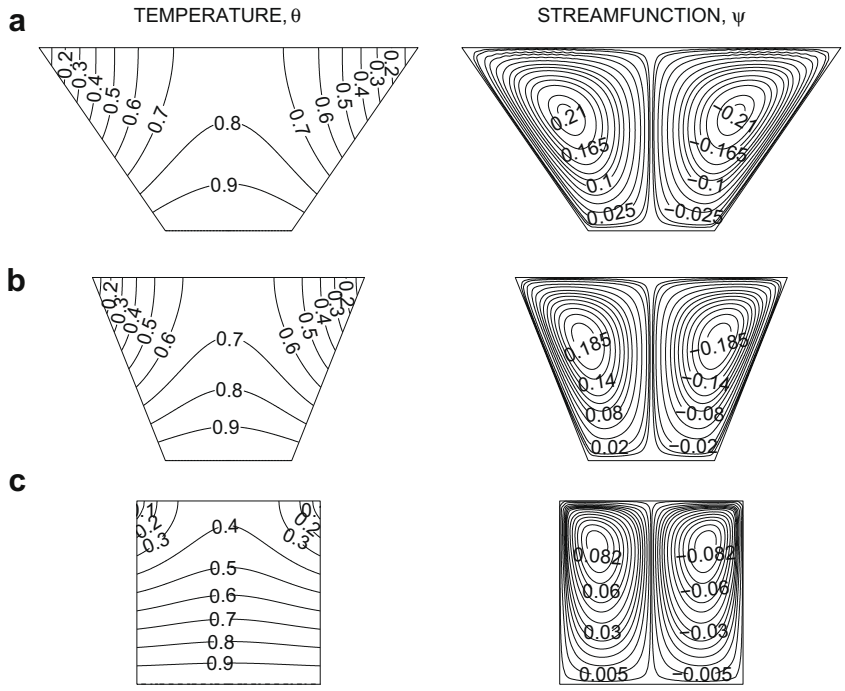

Fig. 2. Isotherms and streamlines for linearly heated side walls with $Pr = 0.026$, $Da = 10^{-5}$ and $Ra = 10^6$ for (a) $\varphi = 45^\circ$, (b) $\varphi = 30^\circ$ and (c) $\varphi = 0^\circ$. Clockwise and anticlockwise flows are shown via negative and positive signs of streamfunctions, respectively.

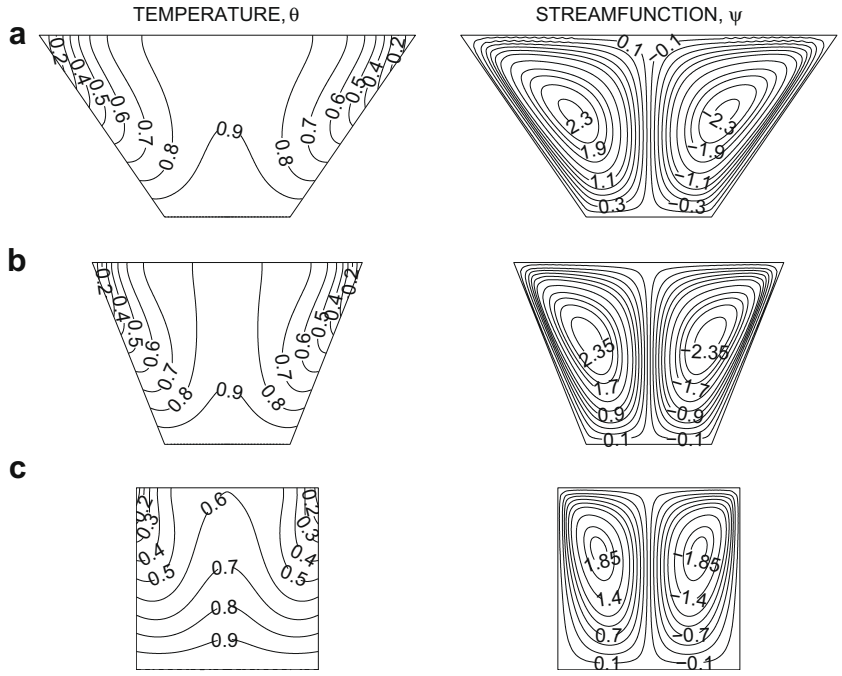

Fig. 3. Isotherms and streamlines for linearly heated side walls with $Pr = 0.026$, $Da = 10^{-4}$ and $Ra = 10^{6}$ for (a) $\varphi = 45°$, (b) $\varphi = 30°$ and (c) $\varphi = 0°$. Clockwise and anti-clockwise flows are shown via negative and positive signs of streamfunctions, respectively.

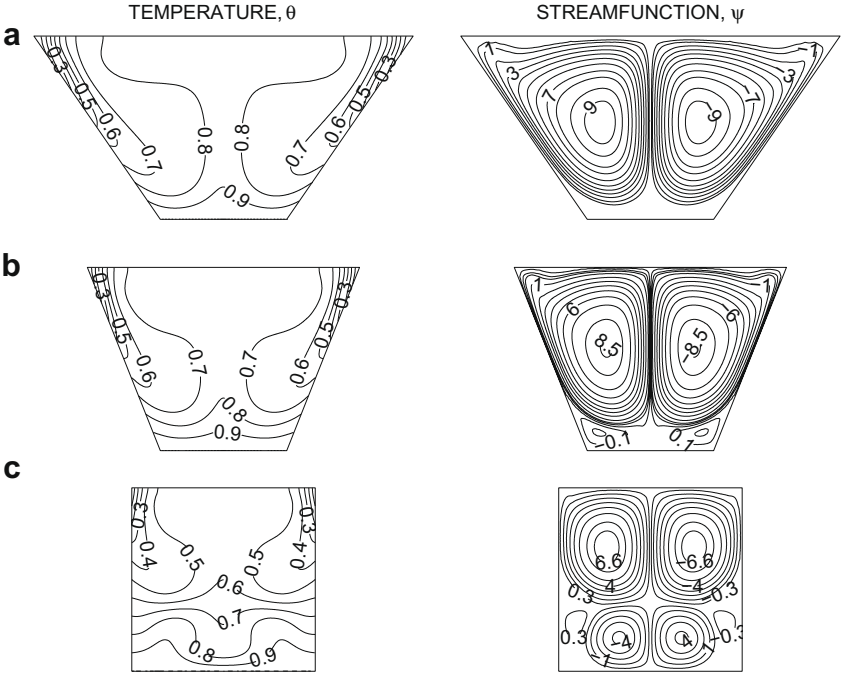

Fig. 4. Isotherms and streamlines for linearly heated side walls with $Pr = 0.026$, $Da = 10^{-3}$ and $Ra = 10^{6}$ for (a) $\varphi = 45°$, (b) $\varphi = 30°$ and (c) $\varphi = 0°$. Clockwise and anti-clockwise flows are shown via negative and positive signs of streamfunctions, respectively.

It is observed that the flow is strongly dependent on *Ra* for $Da = 10^{-3}$. For $Da = 10^{-3}$ and $Ra = 10^{6}$, the circulation near the central regimes become stronger and consequently, the isotherms with $\theta \leqslant 0.8$ for $\varphi = 45°$, $\theta \leqslant 0.7$ for $\varphi = 30°$ and $\theta \leqslant 0.5$ for $\varphi = 0°$ are shifted towards the side walls (see Fig. 4). The intensity of flow circulations for $Pr = 0.026$, $Da = 10^{-3}$ is represented with $|\psi|_{max} = 9$ for $\varphi = 45°$, $|\psi|_{max} = 8.5$ for $\varphi = 30°$ and $|\psi|_{max} = 6.6$ for $\varphi = 0°$.

The greater circulation in each half of the box follows a progressive wrapping around the centers of rotation, and a more and more pronounced compression of isotherms towards the boundary surfaces of the enclosures occurs. The top portions of side walls are found to be cooled as the side walls are linearly heated. It is interesting to observe that the isotherms are highly compressed near the top portions whereas the isotherms are largely dispersed near the bottom portion of side walls and the bottom wall. The large volume of the hot fluid move to the upper regime and a very small regime of the cold section at the side wall receives large amount of heat from the high volume of hot fluid moving from bottom. It is

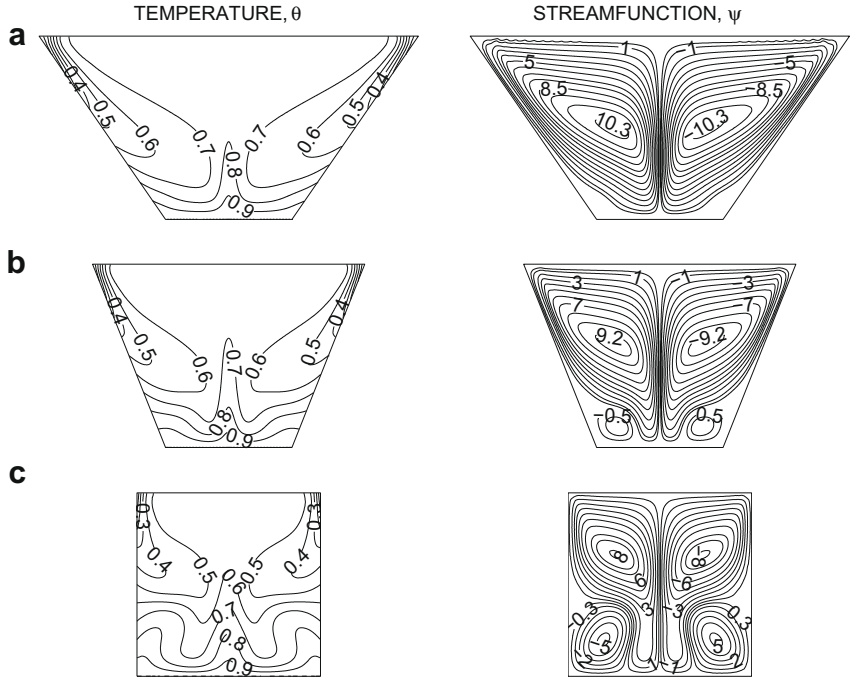

Fig. 5. Isotherms and streamlines for linearly heated side walls with $Pr = 0.7$, $Da = 10^{-3}$ and $Ra = 10^6$ for (a) $\varphi = 45°$, (b) $\varphi = 30°$ and (c) $\varphi = 0°$. Clockwise and anti-clockwise flows are shown via negative and positive signs of streamfunctions, respectively.

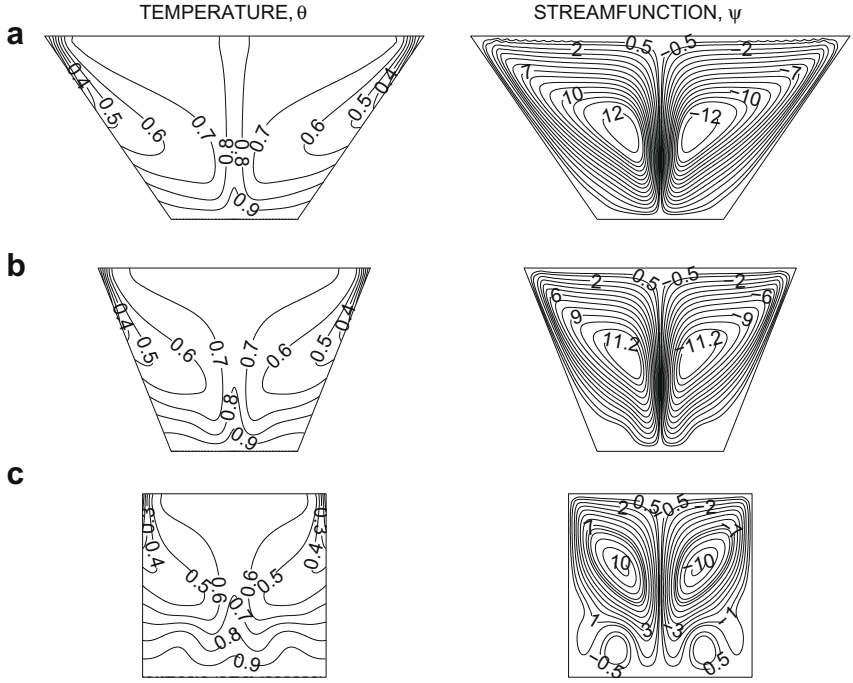

Fig. 6. Isotherms and streamlines for linearly heated side walls with $Pr = 1000$, $Da = 10^{-3}$ and $Ra = 10^6$ for (a) $\varphi = 45°$, (b) $\varphi = 30°$ and (c) $\varphi = 0°$. Clockwise and anti-clockwise flows are shown via negative and positive signs of streamfunctions, respectively.

also interesting to observe that the central regime of the bottom wall corresponds to smallest temperature gradient due to enhanced convection as seen in Fig. 4a–c. It is interesting to note that secondary and tertiary circulations appear at the bottom half of the cavity for $\varphi = 30°$ and $\varphi = 0°$. The secondary circulations pushed the primary circulations towards the upper part of the cavity due to enhanced convection from the hot lower half of the cavity and hot fluid recirculates along the corner of the bottom wall due to secondary circulations. The bottom wall and associated corner regimes show multiple circulations for $\varphi = 0°$ as seen as in Fig. 4c and thus isotherms are found to be non-monotonic in that regime. In addition, the isotherms are also found to be compressed near the central regime of the bottom wall due to strong secondary circulations for $\varphi = 0°$. The number of secondary circulations is found to be also dependent on tilt angle and therefore, the tilt angle plays a significant role on thermal mixing within the fluid. In

fact, with similar parameter values, the secondary circulations disappear for tilt angle, $\varphi > 30^\circ$.

The effect of various Prandtl numbers on isotherms and streamlines are shown in Figs. 4–6. The isotherms with $\theta \leqslant 0.7$ for $\varphi = 45^\circ$, $\theta \leqslant 0.6$ for $\varphi = 30^\circ$ and $\theta \leqslant 0.5$ for $\varphi = 0^\circ$ are compressed towards the side walls for $Pr = 0.026$ and 0.7 (Figs. 4 and 5). The intensity of flow circulations is represented with $|\psi|_{max} = 10.3$ for $\varphi = 45^\circ$, $|\psi|_{max} = 9.2$ for $\varphi = 30^\circ$, $|\psi|_{max} = 8$ for $\varphi = 0^\circ$ for $Pr = 0.7$ whereas the intensity of flow circulations is represented with $|\psi|_{max} = 9$ for $\varphi = 45^\circ$, $|\psi|_{max} = 8.5$ for $\varphi = 30^\circ$ and $|\psi|_{max} = 6.6$ for $\varphi = 0^\circ$ for $Pr = 0.026$. It is also observed that, secondary circulation cells appear at the bottom half of the cavity which pushed the primary circulation cell towards the center of the cavity for $Pr = 0.026$ (Fig. 4c). As Pr increases to 0.7, the secondary circulation cell becomes larger and the intensity of secondary circulations is found to be enhanced (Fig. 5c).

Fig. 6 demonstrates that higher Pr reduces the strength of secondary circulations and simultaneously increases the strength of primary circulations. The secondary circulation disappears for $\varphi \geqslant 30^\circ$ and secondary circulation occurs in a very small zone near the bottom wall for $\varphi = 0^\circ$ (Fig. 6). Due to enhanced strength of primary circulation, thermal mixing is found to be stronger near the top portion of central regime. It is also observed that isotherms along the walls are highly compressed and thickness of the thermal boundary layer is reduced. The intensity of primary circulations for $Pr = 1000$ is represented with $|\psi|_{max} = 12$ for $\varphi = 45^\circ$, $|\psi|_{max} = 11.2$ for $\varphi = 30^\circ$ and $|\psi|_{max} = 10$ for $\varphi = 0^\circ$. The enhanced thermal mixing for $Pr = 1000$ is attributed with $\theta \approx 0.7$–0.8 for $\varphi = 45^\circ$, $\theta \approx 0.7$ for $\varphi = 30^\circ$ and $\theta \approx 0.6$–0.8 for $\varphi = 0^\circ$ at central regimes of the cavities. It may also be remarked that at higher Pr, the shapes of streamlines are found almost trapezoidal near the walls especially for $\varphi \geqslant 30^\circ$ and that signifies enhanced mixing effects.

4.3. Isotherms and streamlines: linearly heated left wall with cold right wall

Figs. 7–10 display the isotherms and streamlines for $Da = 10^{-5}$—10^{-3}, $Ra = 10^6$ and $Pr = 0.026$—1000. Due to uniformly heated bottom wall and cold right wall, the singularity appears at the right bottom edge of the cavity. The formation of the thermal boundary layer along the left wall of the cavity is weaker whereas isotherms are pushed towards the right wall of the cavity forming strong thermal boundary layer. The symmetric circulation pattern which was observed for linearly heated side walls case is absent in the present case due to non-symmetric thermal boundary conditions. Streamlines closer to the top left wall show weaker circulations whereas streamlines closer to the right wall show stronger primary circulations. It may be noted that the uniformly heated bottom wall and linearly heated left wall cause the fluid to move with less circulation along the left wall whereas due to the cooled right wall, larger amount of fluid flow down along the right wall. As a result, strong circulation patterns are formed on the right side of the cavity whereas weaker circulation patterns appear on the left side of the cavity.

For $Pr = 0.026$ with $Ra = 10^6$ and $Da = 10^{-5}$, the magnitude of streamfunction is considerably smaller and the isotherms with $\theta \leqslant 0.6$ for $\varphi = 45^\circ$, $\theta \leqslant 0.5$ for $\varphi = 30^\circ$ and $\theta \leqslant 0.2$ for $\varphi = 0^\circ$ are pushed towards the top corner of the left wall (see Fig. 7). The isotherms are found to be smooth and monotonic and the magnitudes of streamfunction are small illustrating conduction dominant heat transfer. As Da increases to 10^{-3}, the strength of the secondary circulation increases and the primary circulation cell was pushed towards the right corner of the bottom wall (see Fig. 8). The critical Rayleigh number for the conduction dominant mode is found as $Ra = 4 \times 10^4$ for all φ's. At $Ra = 10^6$, $Da = 10^{-3}$ and $Pr = 0.026$, the isotherms with $\theta \leqslant 0.7$ for $\varphi = 45^\circ$, $\theta \leqslant 0.6$ for 30° and $\theta \leqslant 0.5$ for $\varphi = 0^\circ$ are compressed towards the right wall forming strong thermal boundary layer whereas two other thermal boundary layers are formed at top and bottom portion of left walls (Fig. 8a–c). It is observed that the intensity of circulation is large. Note that, $|\psi|_{max}$ is 14 for $\varphi = 45^\circ$, $|\psi|_{max}$ is 14.2 for 30° and $|\psi|_{max}$ is 15.2 for 0°.

Comparative features for various Prandtl numbers ($Pr = 0.7$ and $Pr = 1000$) are shown in Figs. 9 and 10. Increase in Pr does not show much significant change in qualitative trend of streamlines and isotherms in the cavity except that the strength of the circulation increases. It may be noted that $|\psi|_{max} \approx 15.6$ for

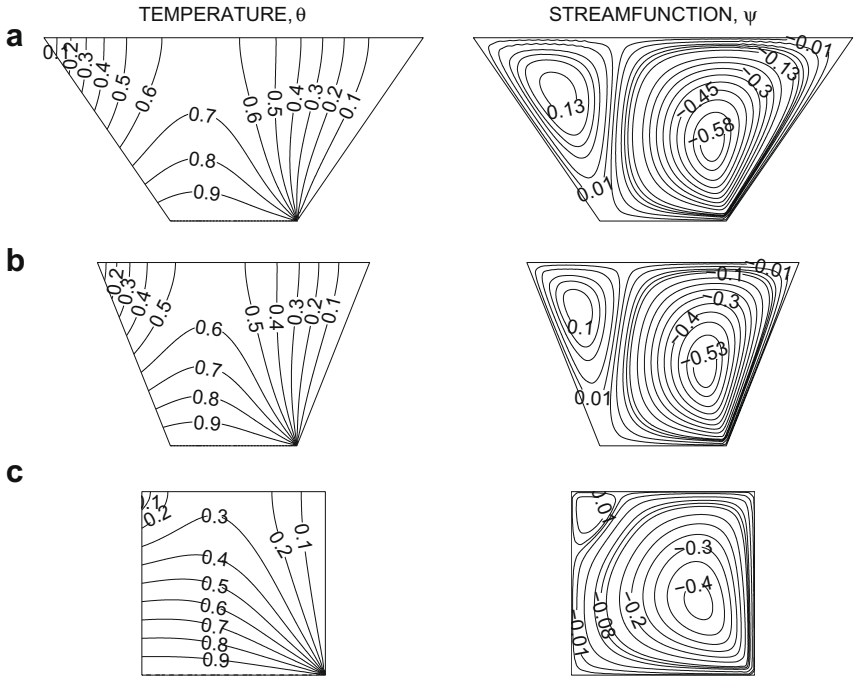

Fig. 7. Isotherms and streamlines for linearly heated left vertical wall and cold right vertical wall with $Pr = 0.026$, $Da = 10^{-5}$ and $Ra = 10^6$ for (a) $\varphi = 45^\circ$, (b) $\varphi = 30^\circ$ and (c) $\varphi = 0^\circ$. Clockwise and anti-clockwise flows are shown via negative and positive signs of streamfunctions, respectively.

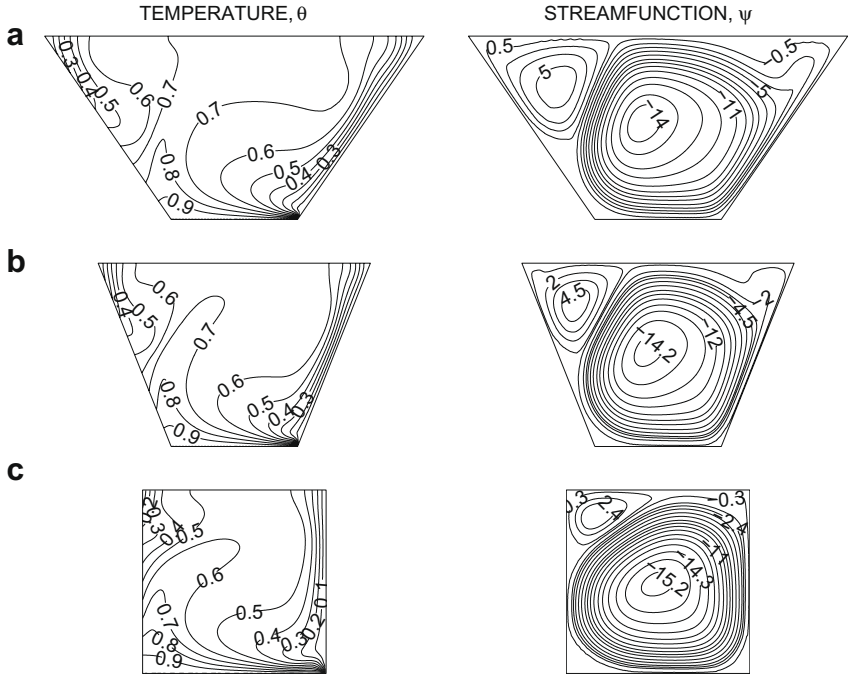

Fig. 8. Isotherms and streamlines for linearly heated left vertical wall and cold right vertical wall with $Pr = 0.026$, $Da = 10^{-3}$ and $Ra = 10^6$ for (a) $\varphi = 45°$, (b) $\varphi = 30°$ and (c) $\varphi = 0°$. Clockwise and anti-clockwise flows are shown via negative and positive signs of streamfunctions, respectively.

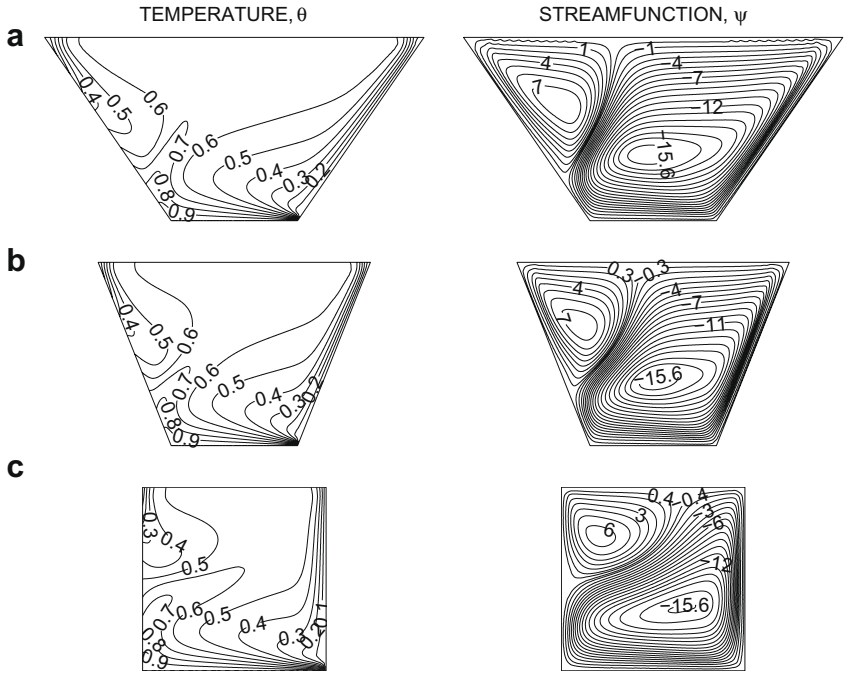

Fig. 9. Isotherms and streamlines for linearly heated left vertical wall and cold right vertical wall with $Pr = 0.7$, $Da = 10^{-3}$ and $Ra = 10^6$ for (a) $\varphi = 45°$, (b) $\varphi = 30°$ and (c) $\varphi = 0°$. Clockwise and anti-clockwise flows are shown via negative and positive signs of streamfunctions, respectively.

all φ's with $Pr = 0.7$ (see Fig. 9) whereas $|\psi|_{max} \approx 17.8$ for all φ's with $Pr = 1000$ (see Fig. 10).

4.4. Heat transfer rates: local Nusselt numbers

4.4.1. Case I: linearly heated side walls

Fig. 11 displays the local heat transfer rates (Nu_b, Nu_s) for $Pr = 0.026$ and $Pr = 1000$ with $Ra = 10^6$ and $Da = 10^{-5}$–10^{-3} involving various tilt angles (φ). Due to the symmetry in the temperature field, heat transfer at the bottom wall is symmetric with respect to the midlength $(X = 1/2)$. Fig. 11a–c illustrates local Nusselt number distribution at the bottom wall (Nu_b) for $\varphi = 45°$, 30° and 0°, respectively. Due to linearly heated side walls, the heat transfer rate, Nu_b, is 1 at the edges of the bottom wall. For $Da = 10^{-5}$ with $Pr = 0.026$, due to less intensity of circulation, the isotherms are almost parallel to the bottom wall for all tilt angles as seen in Fig. 2. It is also observed that the zone of thermal stratification or thermal gradient is largest for $\varphi = 0°$. On the other hand, the

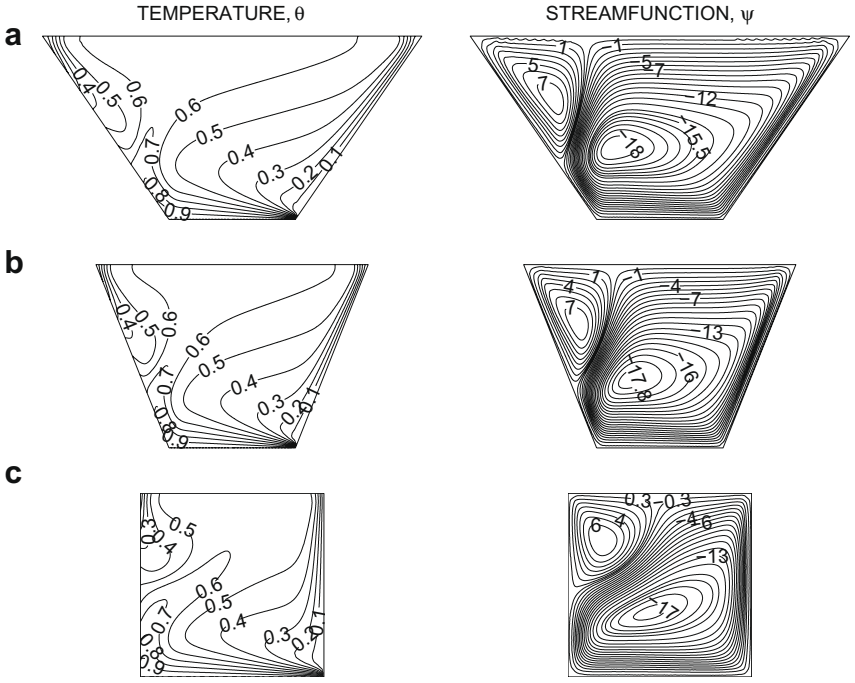

Fig. 10. Isotherms and streamlines for linearly heated left vertical wall and cold right vertical wall with $Pr = 1000$, $Da = 10^{-3}$ and $Ra = 10^{6}$ for (a) $\varphi = 45°$, (b) $\varphi = 30°$ and (c) $\varphi = 0°$. Clockwise and anti-clockwise flows are shown via negative and positive signs of streamfunctions, respectively.

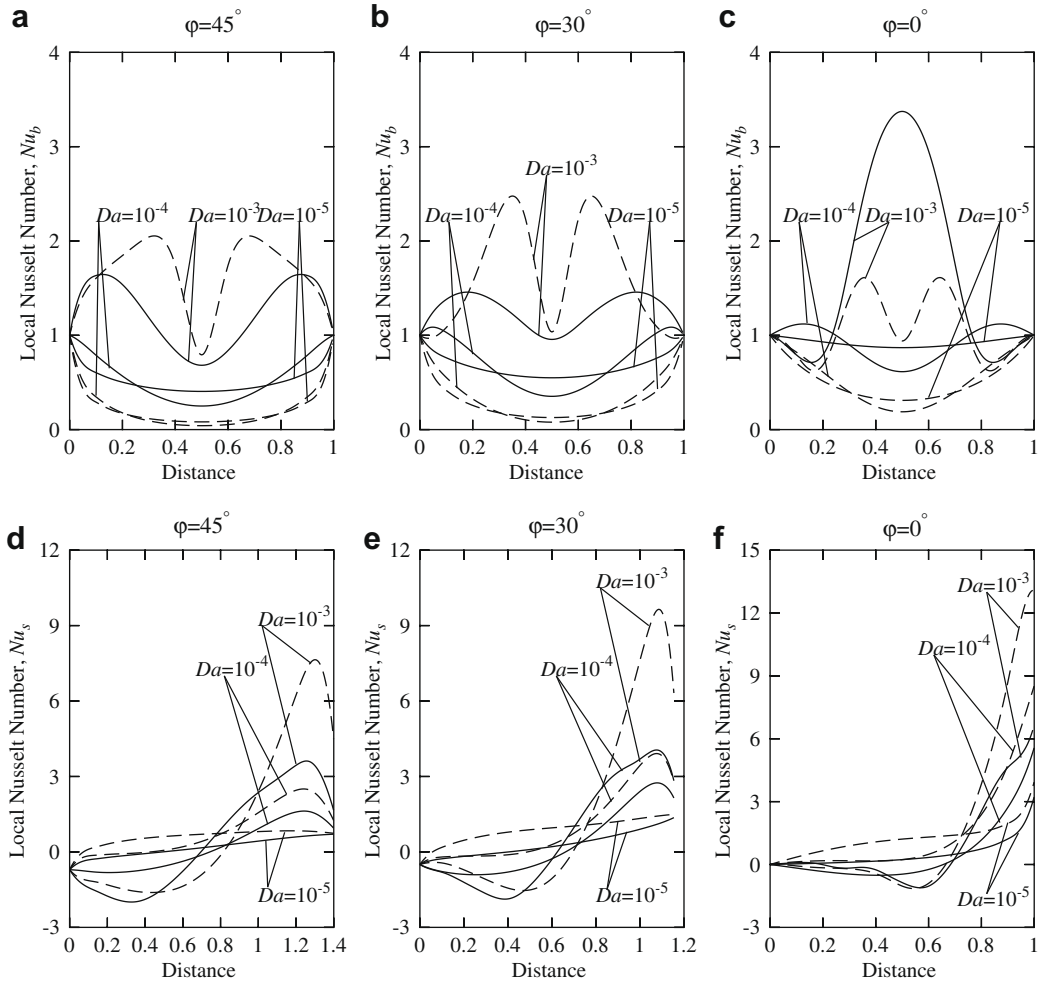

Fig. 11. Variation of local Nusselt number with distance along (a)–(c) for bottom wall; (d)–(f) for side wall for $\varphi = 45°$, $\varphi = 30°$ and $\varphi = 0°$, with $Pr = 0.026$ (—) and $Pr = 1000$ (- - - - -) for $Da = 10^{-5}$—10^{-3} at $Ra = 10^{6}$ in presence of linearly heated side walls.

thermal gradient is almost zero along the entire bottom wall especially for $\varphi = 45°$ and 30° at $Pr = 1000$. Similar to $Pr = 0.026$, Nu_b is largest for $\varphi = 0°$ for $Pr = 1000$. Overall, Nu_b for $Pr = 1000$ is lesser than that for $Pr = 0.026$ for all tilt angles (see Fig. 11a–c). Common to $Pr = 0.026$ and 1000, Nu_b exhibits a local minima at the center of the bottom wall and that has maxima at the corner points of the bottom wall. The convection starts playing a dominant role for $Da = 10^{-4}$ with $Pr = 0.026$ and the isotherms are pushed towards the side walls. It is interesting to observed that for $Pr = 0.026$, the heat transfer rate, Nu_b, follows sinusoidal variation with its minimum value at the center of the bottom wall and this trend is in accord with sinusoidal variation of isotherms near the bottom wall. On the other hand, for $Pr = 1000$, isotherms are highly compressed towards side walls and they are highly dispersed near the bottom wall similar to $Da = 10^{-5}$ and therefore qualitatively similar Nu_b distributions are observed for $Da = 10^{-5}$ and 10^{-4} in presence of $Pr = 1000$ with all tilt angles.

At $Da = 10^{-3}$, Nu_b is found to be larger than that for $Da = 10^{-5}$ and 10^{-4} with both Pr ($Pr = 0.026$ and 1000). The sinusoidal or non-monotonic variation of Nu_b distribution is also observed for $Da = 10^{-3}$. It is interesting to observe that due to enhanced circulation, isotherms are largely compressed near the middle portion of the bottom wall for $Pr = 1000$ with $\varphi = 45°$ and 30° (see Fig. 6a and b) and the magnitude of Nu_b is larger at the middle portion for $Pr = 1000$ with $\varphi = 45°$ and 30°. On the other hand, Nu_b for $Pr = 0.026$ is much larger than that for $Pr = 1000$ at the middle portion of the bottom wall with $\varphi = 0°$. The larger value of Nu_b with $Pr = 0.026$ is due to large compression of isotherms resulting from multiple circulations as seen in Fig. 4c whereas the strength of multiple circulations near the bottom wall is smaller for $Pr = 1000$ as seen in Fig. 6c.

Heat transfer rates for linearly heated side walls at $Da = 10^{-5}$– 10^{-3}, $Ra = 10^6$ with $Pr = 0.026$ and $Pr = 1000$ are illustrated in Fig. 11d–f for various tilt angles. Due to the symmetry in the boundary condition, the local Nusselt number, Nu_s, is identical along both the side walls. For $Da = 10^{-5}$ with $Pr = 0.026$, isotherms are disperse and uniform and the heat transfer rate (Nu_s) is almost zero up to $Y = 0.7$ and Nu_s is large near the top corner for all tilt angles. It may be noted that Nu_s is larger for $Pr = 1000$ compared to $Pr = 0.026$ due to more compressed isotherms towards the side walls at $Da = 10^{-5}$ for all tilt angles. Due to stronger circulations, the heat transfer rate (Nu_s) is larger for $Da = 10^{-4}$ with $Pr = 0.026$ near the top corner than those with $Da = 10^{-5}$ for all tilt angles. The heat transfer rate is even larger for $Pr = 1000$. Due to stronger circulations near the top portion, the increasing trend of heat transfer rate is observed in the upper half of the side walls at $Da = 10^{-3}$ for $\varphi = 45°$, 30° and 0°. It is interesting to note that Nu_s is quite large for $Pr = 1000$ compared to $Pr = 0.026$ at 10^{-3} due to highly compressed isotherms near the top portion of the side walls for all tilt angles (see Figs. 4 and 6). Due to presence of a pair of symmetric secondary circulation cells with clockwise and anti-clockwise rotations for $\varphi = 0°$ and $Da = 10^{-3}$, the heat transfer rate is non-monotonic in nature in the lower half of the side walls, but the increasing trend of heat transfer rate is observed in the upper half of the side walls. Local Nusselt number being negative near the bottom portion of side walls implies that part of the heat goes into the lower part of the wall for $\varphi = 45°$ and 30° whereas for $\varphi = 0°$, the local Nusselt number (Nu_s) is almost zero at the bottom edge of the side wall due to isotherms parallel to the bottom wall.

4.4.2. Case II: linearly heated left wall with cold right wall

Fig. 12 displays the local Nusselt numbers at the bottom, left and right walls (Nu_b, Nu_l, Nu_r) for $Pr = 0.026$ and $Pr = 1000$ with $Da = 10^{-5}$–10^{-3} and $Ra = 10^6$ for various tilt angles (φ). For all the cases, the isotherms near the bottom-edge of the cold right wall are compressed due to the discontinuity present in the right-edge resulting in high thermal gradient near the right-edge of the bottom wall. The heat transfer rate (Nu_b) is 1 at the left-edge of the bottom wall due to linearly heated left wall and that is maximum at the right-edge of the bottom wall due to the cold right wall for all φ's (see Fig. 12a–c). It is observed that the local Nusselt number (Nu_b) increases with the distance along the bottom wall, but as Pr increases from 0.026 to 1000, local Nusselt number (Nu_b) has lesser value due to less dense isotherms near the right end of the bottom wall for $Pr = 1000$ at $Da = 10^{-5}$ with all tilt angles. The heat transfer rate (Nu_b) is larger for $Da = 10^{-4}$ compared to $Da = 10^{-5}$ due to increase of strength of circulations with $Pr = 0.026$ and 1000. It may be noted that, the distribution of Nu_b for $Da = 10^{-4}$ is almost invariant of Pr with all tilt angles (Fig. 12a–c). Similar qualitative trend in Nu_b is observed for $Da = 10^{-3}$. It is interesting to observe that enhanced anti-clockwise primary circulation cell compresses isotherms near the left corner of bottom wall for $Pr = 1000$ and Nu_b is larger near the left corner for $Pr = 1000$.

Fig. 12d–f illustrates the heat transfer rate (Nu_l) for the left wall. Fig. 12d and e shows that Nu_l is negative at the bottom edge indicating the heat transfer occurs from fluid to the left wall for $\varphi = 30°$ and 45°. But, for $\varphi = 0°$ (Fig. 12f) the heat transfer rate at the bottom edge of the left wall is zero. An increasing trend in Nu_l is observed from the bottom edge to the top edge of the left wall for all tilt angles at $Da = 10^{-5}$–10^{-4}. Local Nusselt number Nu_l for $Pr = 1000$ is large compared to $Pr = 0.026$ due to largely compressed isotherms towards the top edge of the left wall. Due to the presence of secondary circulations near the left wall, the local Nusselt number exhibits non-monotonic trend except near the top edge at $Da = 10^{-3}$. Further, the secondary circulations push isotherms at the top edge of the left wall leading to larger temperature gradient which result in large local Nusselt number. For $\varphi = 0°$ (Fig. 12f), the magnitude of heat transfer rate (Nu_l) is large for $Y \geqslant 0.75$ with $Da = 10^{-3}$. This is due to presence of strong circulations at top portion of left wall. As Pr increases from 0.026 to 1000, due to enhanced viscous effect, the intensity of both primary and secondary circulations increases and isotherms are highly compressed towards the top portion of left wall especially for $\varphi = 0°$, Fig. 10. It is found that Nu_l for $Pr = 1000$ is found to be large compared to $Pr = 0.026$ near the top edge of the left wall with $Da = 10^{-3}$ and for all φ's.

Fig. 12g–i illustrates the local heat transfer rate (Nu_r) at the right wall. Due to the singularities present in the thermal boundary condition at the right corner of the bottom wall, the heat transfer rate is maximum at the bottom edge of the right wall. At $Da = 10^{-5}$, Nu_r is found to decrease continuously due to increase in thermal boundary layer thickness towards top portion of right wall with $Pr = 0.026$ and $Pr = 1000$ for all tilt angles. At $Da = 10^{-4}$, Nu_r first decreases and that increases slightly for $Y \geqslant 0.2$ due to compression of isotherms and thereafter Nu_r decreases due to large thickness of thermal boundary larger at the top edge with $Pr = 0.026$ and $Pr = 1000$ for $\varphi = 45°$ and 30° except for $\varphi = 0°$, which correspond to increasing function of Nu_r near the top edge. Similar qualitative trend of Nu_r is observed for $Da = 10^{-3}$. It is also observed that Nu_r is large for $Pr = 1000$ compared to $Pr = 0.026$ due to high intensity of primary circulations and highly compressed boundary layers thickness at top portion of side wall for $Da = 10^{-3}$.

4.5. Overall heat transfer and average Nusselt numbers

4.5.1. Case I: linearly heated side walls

The overall effects upon the heat transfer rates are displayed in Fig. 13a–d where the distributions of the average Nusselt number of the bottom and side walls vs. the logarithmic Rayleigh number are plotted. The average Nusselt numbers are obtained using Eqs.

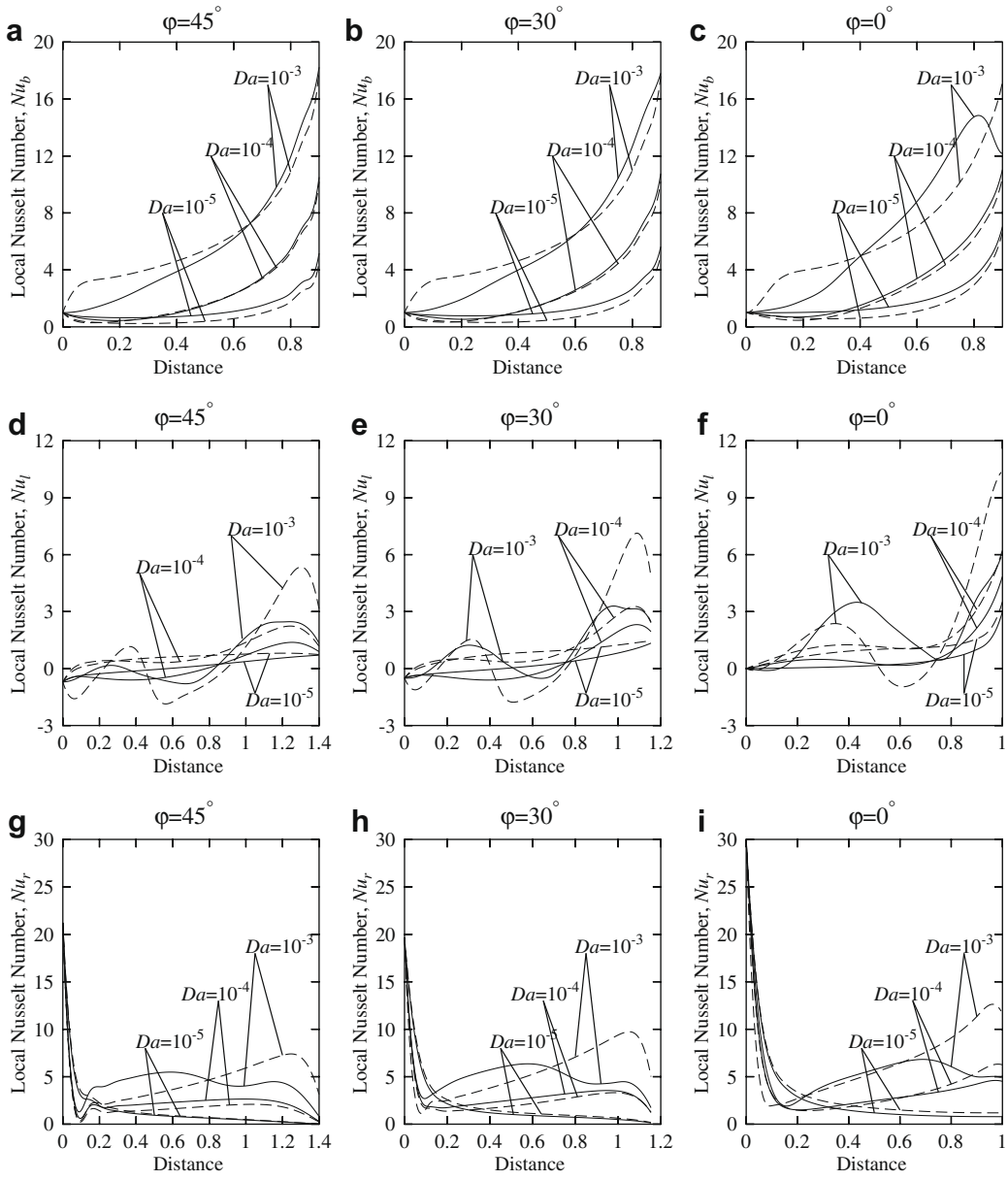

Fig. 12. Variation of local Nusselt number with distance along (a)–(c) for bottom wall; (d)–(f) for left wall and (g)–(i) for right wall for $\varphi = 45°$, $\varphi = 30°$ and $\varphi = 0°$, with $Pr = 0.026$ (—) and $Pr = 1000$ (-----) for $Da = 10^{-5}$–10^{-3} at $Ra = 10^6$ in presence of linearly heated left wall and cold right wall.

(14)–(16) where the integral is evaluated using Simpson's 1/3 rule. It is observed that at $Da = 10^{-5}$ with $Pr = 0.026$, the average Nusselt number ($\overline{Nu_b}$) is constant for the entire range of Ra with all tilt angles and that signifies conduction dominant mode (see lower panel of Fig. 13a). For $Da = 10^{-5}$ with $Pr = 1000$, $\overline{Nu_b}$ remains constant up to $Ra = 8 \times 10^4$ and thereafter that starts to decrease smoothly as very small thermal gradient occurs near the central regime of the bottom wall at higher Ra (see lower panel of Fig. 13b). It is observed that the intensity of both primary and secondary cells increases at higher Ra, and as a result, isotherms start to shift from bottom wall towards side wall. Therefore, convection shows dominant mode of heat transfer at high Ra for $Pr = 1000$ and $Da = 10^{-5}$. The upper panels for Fig. 13a and b represent $\overline{Nu_b}$ for $Da = 10^{-3}$. It is observed that $\overline{Nu_b}$ remains constant up to $Ra = 6 \times 10^4$ for $Da = 10^{-3}$ with $Pr = 0.026$ and $Pr = 1000$ and thereafter that smoothly increases with the increase of Rayleigh numbers especially for $\varphi = 45°$ and 30° (see upper panels of Fig. 13a and b). It is interesting to note that $\overline{Nu_b}$ sharply increases at $Ra = 6 \times 10^5$ for $Pr = 0.026$ whereas for $Pr = 1000$, average Nusselt numbers decreases with Ra at $Ra \geqslant 6 \times 10^5$ due to secondary circulations at $\varphi = 0°$ (upper panels of Fig. 13a and b).

Fig. 13c and d displays $\overline{Nu_s}$ for $Pr = 0.026$ and 1000, respectively. It is interesting to observe that the values of $\overline{Nu_s}$ along the side walls are less compared to $\overline{Nu_b}$. This is due to the fact that the heat transfer to the fluid from the hot bottom wall is more compared to that of linearly heated side wall. For $Da = 10^{-5}$ with $Pr = 0.026$, the average Nusselt number is constant irrespective of Ra for all tilt angles, illustrating conduction dominant mode (see lower panel of Fig. 13c). For $Da = 10^{-5}$ with $Pr = 1000$, the average Nusselt number remains constant up to $Ra = 8 \times 10^4$ and that increases smoothly due to large compression of isotherms towards side wall as Ra increases (see lower panel of Fig. 13d). It is observed that at $Da = 10^{-3}$, the average Nusselt number for side wall remains constant up to $Ra = 10^5$ for both $Pr = 0.026$ and 1000 and thereafter that increases with the increase of Ra for all tilt angles (upper panels of Fig. 13c and d). Similar to bottom wall, the influence of the Rayleigh number on the average Nusselt number becomes more significant at higher Darcy number as seen in the upper panel of

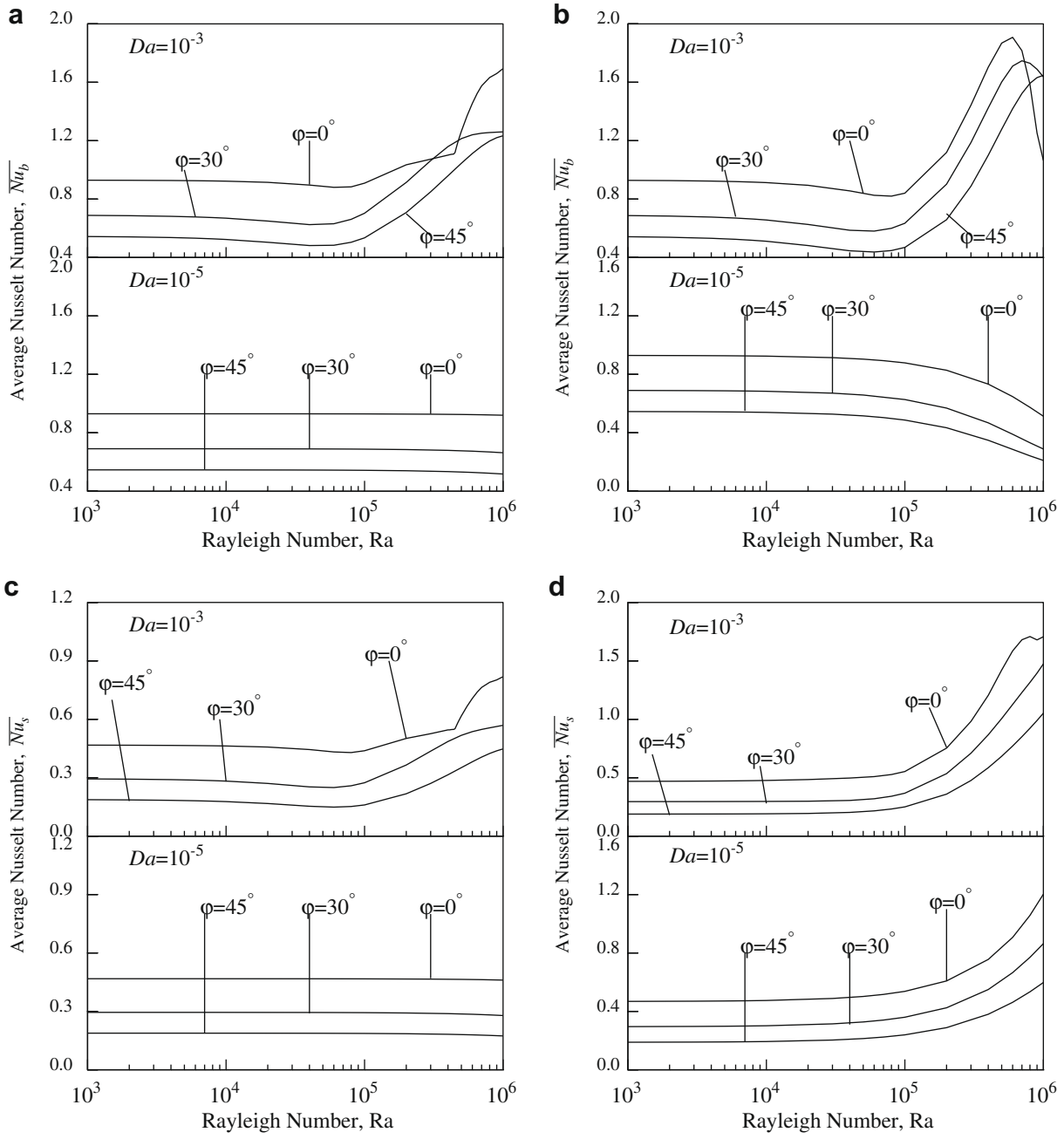

Fig. 13. Variation of average Nusselt number with Rayleigh number for linearly heated side walls. Panels (a) and (b) represent $\overline{Nu}_b$ with $Pr = 0.026$ and $Pr = 1000$, respectively, and panels (c) and (d) represent $\overline{Nu}_s$ with $Pr = 0.026$ and $Pr = 1000$, respectively. In each plot, upper panel corresponds to $Da = 10^{-3}$ and lower panel represents $Da = 10^{-5}$.

Fig. 13c and d. It is interesting to observe that the monotonic increasing trend of $\overline{Nu}_s$ is not observed for $\varphi = 0°$ at higher *Ra* and similar trend also has been observed for the bottom wall. Therefore, power law correlations for $\overline{Nu}_b$ and $\overline{Nu}_s$ are not obtained.

4.5.2. Case II: linearly heated left wall with cold right wall

The overall effects of *Ra*, *Da* and *Pr* on the average Nusselt numbers at the bottom, left and right walls are displayed in Fig. 14a–d. At $Da = 10^{-5}$ with $Pr = 0.026$ the average Nusselt numbers at the bottom wall remain constant for entire *Ra* range indicating conduction dominant mode for all tilt angles (see lower panel of Fig. 14a). For $Da = 10^{-5}$ with $Pr = 1000$, $\overline{Nu}_b$ remains constant up to $Ra = 10^5$ and thereafter that starts to decrease slightly as the isotherms near the left wall are pulled up due to strong secondary circulation for all tilt angles at higher *Ra* (see lower panel of Fig. 14b). At $Da = 10^{-3}$, the average Nusselt numbers for bottom wall remain constant up to $Ra = 2 \times 10^4$, thereafter $\overline{Nu}_b$ smoothly increases with *Ra* for all φ with $Pr = 0.026$ and 1000 (see upper panels of Fig. 14a and b).

The average Nusselt numbers for the side walls remain almost constant up to $Ra = 10^6$ indicating conduction dominant mode for all tilt angles (see lower panel of Fig. 14c) with $Da = 10^{-5}$ and $Pr = 0.026$. But, For $Da = 10^{-5}$ with $Pr = 1000$, the average Nusselt numbers at the side walls remain almost constant up to $Ra = 5 \times 10^5$, thereafter that increases smoothly for all tilt angles due to larger compression of isotherms near side walls. It is observed that $\overline{Nu}_l$ increases sharply with *Ra* for $\varphi \leqslant 30°$ for

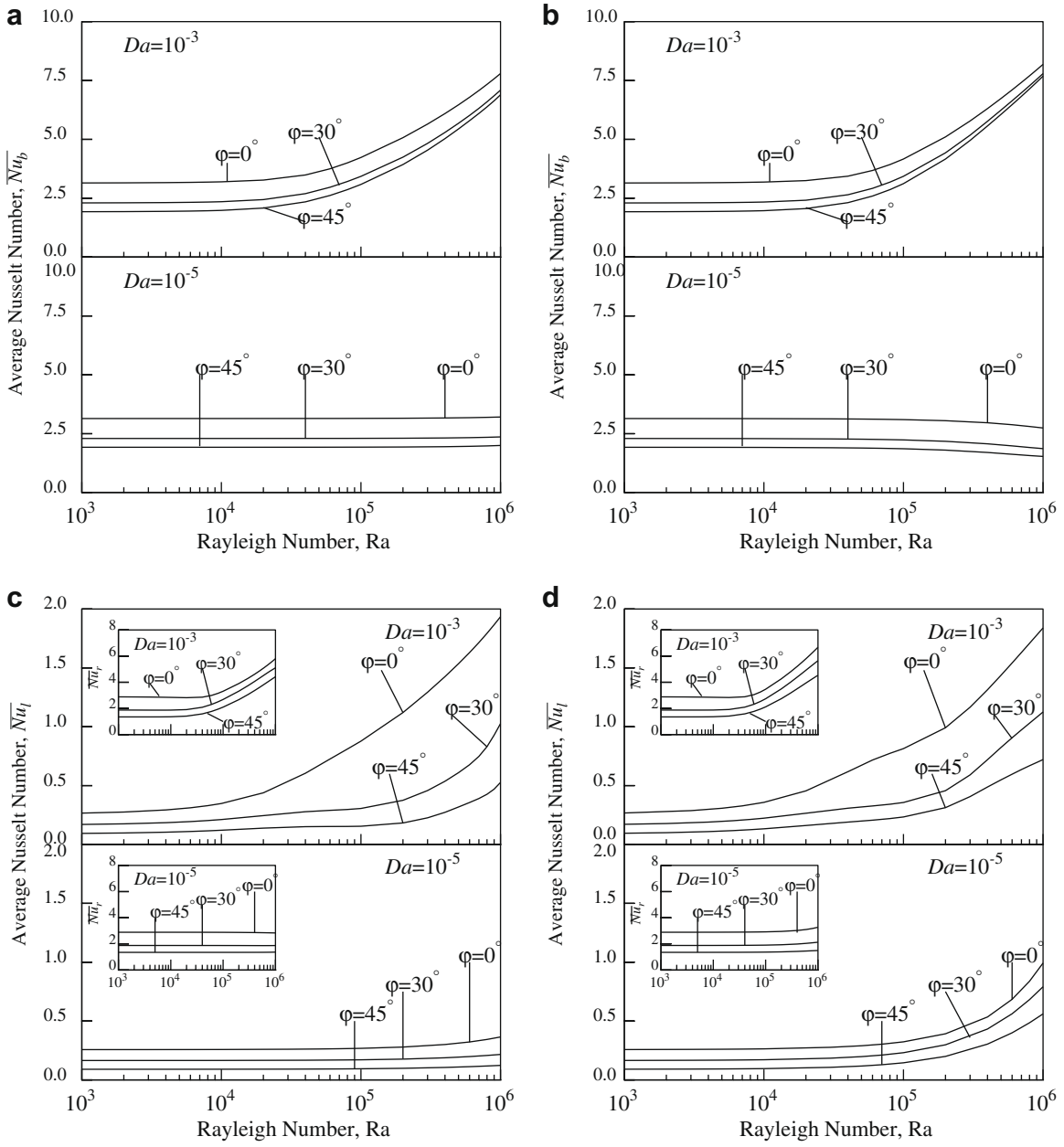

Fig. 14. Variation of average Nusselt number with Rayleigh number for linearly heated left wall and cold right wall. Panels (a) and (b) represent $\overline{Nu}_b$ with $Pr = 0.026$ and $Pr = 1000$, respectively, and panels (c) and (d) represent $\overline{Nu}_l$ with $Pr = 0.026$ and $Pr = 1000$, respectively. The insets show the plot of average Nusselt number vs. Rayleigh number for $\overline{Nu}_r$. In each plot, upper panel corresponds to $Da = 10^{-3}$ and lower panel represents $Da = 10^{-5}$.

Pr = 0.026 and 1000 (see upper panel of Fig. 14c and d). The sharp increase of $\overline{Nu}_l$ is due to large compression of isotherms near the top portion of the left wall due to secondary circulations. The inset of Fig. 14c and d displays the variation of average Nusselt number of right wall ($\overline{Nu}_r$). It is observed that $\overline{Nu}_r$ remains constant up to $Ra = 4 \times 10^4$ for φ = 45°, 30° and 0° then increases smoothly with Rayleigh number for all φ at $Da = 10^{-3}$ due to larger compression of isotherms caused by a primary circulation cell. It is interesting to observe that the magnitude of $\overline{Nu}_r$ is larger than those of $\overline{Nu}_l$ for all range of Ra, Pr and Da as the entire cold right wall receives large amount of heat at steady state.

5. Conclusion

The effect of linearly heated side wall(s) and uniformly heated bottom wall on flow and heat transfer characteristics due to natural convection in porous medium within the trapezoidal enclosure have been studied in details. The momentum transfer in the porous region is modeled using Darcy–Forchheimer principle with Forchheimer inertia term being neglected. The penalty finite element method is used to obtain smooth solutions in terms of streamlines and isotherms for a wide ranges of Pr, Ra and Da. Numerical simulations are performed for various values of Rayleigh, Prandtl and Darcy numbers ($10^3 \leqslant Ra \leqslant 10^6$, $0.026 \leqslant Pr \leqslant 1000$ and $10^{-5} \leqslant Da \leqslant 10^{-3}$) and side wall inclination angles (φ = 45°, 30° and 0°). During conduction dominant heat transfer, variation of tilt angles from φ = 45° to φ = 0° has less significance. Stronger convection is observed for φ = 45°, 30° than that for φ = 0° with $Pr = 0.026$, $Ra = 10^6$ and $Da = 10^{-3}$. The secondary circulations are observed near the bottom corner for φ = 30° and 0° with linearly heated side walls. In contrast, stronger circulations are observed near the top portion of the left wall with

linearly heated left wall and cold right wall. As *Pr* increases from 0.026 to 1000, the circulations become stronger which results in larger compression of isotherms near various regimes of the walls.

It is observed that the heat transfer rate (Nu_b), for $Pr = 1000$ is less compared to $Pr = 0.026$ at $Da = 10^{-5}$ for all tilt angles. But, for $Da = 10^{-4}$ with $Pr = 0.026$, convection starts playing a dominant role showing non-monotonic variation of Nu_b with minimum value at center whereas for $Pr = 1000$ with $Da = 10^{-4}$, Nu_b is found to be similar to that with $Da = 10^{-5}$. It is interesting to note that for $Da = 10^{-3}$, sinusoidal variation in Nu_b is observed with large values than those at $Da = 10^{-5}$ and 10^{-4}. It is observed that Nu_b for $Pr = 1000$ is larger than that for $Pr = 0.026$ at $\varphi = 45^\circ$ and 30° but for $\varphi = 0^\circ$, Nu_b with $Pr = 0.026$ is larger due to large compression of isotherms resulting from multiple circulations. Due to stronger circulations near the top portion, the increasing trend of heat transfer rate (Nu_s) is observed in the upper half of the side walls at $Da = 10^{-3}$ than that at $Da = 10^{-5}$ and 10^{-4} for all tilt angles. It is observed that Nu_s is larger for $Pr = 1000$ compared to $Pr = 0.026$ at $Da = 10^{-3}$ due to highly compressed isotherms near the top portion of the side walls for all tilt angles.

Interesting heat transfer characteristics are also observed for linearly heated left wall and cold right wall. The local Nusselt number (Nu_b) increases with the distance along the bottom wall. As *Da* increases to 10^{-3}, Nu_b also increases due to increase in strength of circulations for $Pr = 0.026$ and 1000. An increasing trend in Nu_l is observed from the bottom edge to the top edge of the left wall for all tilt angles at $Da = 10^{-5}$—10^{-4}. Due to the presence of secondary circulations near the left wall, the local Nusselt number exhibits non-monotonic trend except near the top edge at $Da = 10^{-3}$. Overall, Nu_l for $Pr = 1000$ is found to be larger compared to $Pr = 0.026$ with all Darcy number for all φ's. Due to the singularities present in the thermal boundary condition at the right corner of the bottom wall, the heat transfer rate is maximum at the bottom edge of the right wall. At $Da = 10^{-5}$, Nu_r is found to decrease continuously due to increase in thermal boundary layer thickness towards top portion of right wall with $Pr = 0.026$ and $Pr = 1000$ for all tilt angles. But for $Da = 10^{-4}$—10^{-3}, Nu_r first decreases and that increases slightly for $Y \geqslant 0.2$ and thereafter Nu_r decreases with $Pr = 0.026$ and $Pr = 1000$ for $\varphi = 45^\circ$ and 30° except for $\varphi = 0^\circ$, which correspond to increasing function of Nu_r.

It is observed that average Nusselt number ($\overline{Nu_b}$) sharply decreases at higher *Ra* for $Pr = 1000$ and $Da = 10^{-5}$ with linearly heated side walls, but $\overline{Nu_b}$ slowly decreases at higher *Ra* with $Da = 10^{-5}$ due to linearly heated left wall for all tilt angles. For all other cases, average Nusselt number is a monotonically increasing function of *Ra* especially for higher *Da* ($Da \geqslant 10^{-4}$) except with some cases for $\varphi = 0^\circ$ due to linearly heated side walls.

References

[1] O.G. Martynenko, P.P. Khramtsov, Free-Convective Heat Transfer, Springer, Berlin, 2005.

[2] C.W. Lei, J.C. Patterson, Natural convection in a reservoir sidearm subject to solar radiation: a two-dimensional simulation, Numer. Heat Transfer A 42 (2002) 13–32.

[3] H.Y. Miao, B. Milton, Numerical simulation of the gas/diesel dual-fuel engine in-cylinder combustion process, Numer. Heat Transfer A 47 (2005) 523–547.

[4] K.C. Tseng, J.R. Tsai, Numerical solver for an ultrafast laser heating on different 3-D microscale metallic films, Numer. Heat Transfer A 53 (2008) 726–748.

[5] F. Joly, O. Quemener, A. Neveu, Modal reduction of an advection-diffusion model using a branch basis, Numer. Heat Transfer B 53 (2008) 466–485.

[6] M. Molki, T. Harirchian, V.L. Chitta, An improved solution of electrodynamics equations for corona discharge using explicit artificial viscosity, Numer. Heat Transfer B 50 (2006) 315–332.

[7] S. Are, S.H. Hou, D.P. Schmidt, Second-order spatial accuracy in Lagrangian–Eulerian spray calculations, Numer. Heat Transfer B 48 (2005) 25–44.

[8] T. Fusegi, J.M. Hyun, K. Kuwahara, Natural-convection in a differentially heated square cavity with internal heat-generation, Numer. Heat Transfer A 21 (1992) 215–229.

[9] J.L. Lage, A. Bejan, The *Ra–Pr* domain of laminar natural-convection in an enclosure heated from the side, Numer. Heat Transfer A 19 (1991) 21–41.

[10] J.L. Lage, A. Bejan, The resonance of natural-convection in an enclosure heated periodically from the side, Int. J. Heat Mass Transfer 36 (1993) 2027–2038.

[11] C.M. Xia, J.Y. Murthy, Buoyancy-driven flow transitions in deep cavities heated from below, Trans. ASME J. Heat Transfer 124 (2002) 650–659.

[12] A. Bejan, D. Poulikakos, The non-Darcy regime for vertical boundary-layer natural-convection in porous-medium, Int. J. Heat Mass Transfer 27 (1984) 717–722.

[13] D.A. Nield, A. Bejan, Convection in Porous Media, third ed., Springer, New York, 2006.

[14] D.B. Ingham, I. Pop, Transport Phenomena in Porous Media, Pergamon Press, New York, 1998.

[15] A.M. Al-Amiri, Natural convection in porous enclosures: the application of the two-energy equation model, Numer. Heat Transfer A 41 (2002) 817–834.

[16] A.A. Merrikh, A.A. Mohamad, Non-Darcy effects in buoyancy driven flows in an enclosure filled with vertically layered porous media, Int. J. Heat Mass Transfer 45 (2002) 4305–4313.

[17] X.B. Chen, P. Yu, S.H. Winoto, H.T. Low, Free convection in a porous wavy cavity based on the Darcy–Brinkman–Forchheimer extended model, Numer. Heat Transfer A 52 (2007) 377–397.

[18] H.C. Brinkman, On the permeability of media consisting of closely packed porous particles, Appl. Sci. Res. 1 (1947) 81–86.

[19] D. Poulikakos, A. Bejan, The departure from Darcy flow in natural-convection in a vertical porous layer, Phys. Fluids 28 (1985) 3477–3484.

[20] G. Lauriat, V. Prasad, Non-Darcian effects on natural-convection in a vertical porous enclosure, Int. J. Heat Mass Transfer 32 (1989) 2135–2148.

[21] B.M.D. Miranda, N.K. Anand, Convective heat transfer in a channel with porous baffles, Numer. Heat Transfer A 46 (2004) 425–452.

[22] A. Al-Amiri, K. Khanafer, I. Pop, Steady-state conjugate natural convection in a fluid-saturated porous cavity, Int. J. Heat Mass Transfer 51 (2008) 4260–4275.

[23] T. Basak, S. Roy, T. Paul, I. Pop, Natural convection in a square cavity filled with a porous medium: effects of various thermal boundary conditions, Int. J. Heat Mass Transfer 49 (2006) 1430–1441.

[24] Y. Varol, H.F. Oztop, I. Pop, Numerical analysis of natural convection for a porous rectangular enclosure with sinusoidally varying temperature profile on the bottom wall, Int. Commun. Heat Mass Transfer 35 (2008) 56–64.

[25] G.B. Kim, J.M. Hyun, H.S. Kwak, Buoyant convection in a square cavity partially filled with a heat-generating porous medium, Numer. Heat Transfer A 40 (2001) 601–618.

[26] W.J. Chang, D.F. Yang, Transient natural-convection of water near its density extremum in a rectangular cavity filled with porous-medium, Numer. Heat Transfer A 28 (1995) 619–633.

[27] M.W. Waite, M.R. Amin, Numerical investigation of two-phase fluid flow and heat transfer in porous media heated from the side, Numer. Heat Transfer A 35 (1999) 271–290.

[28] S. Kiwan, M.S. Alzahrany, Effect of using porous inserts on natural convection heat transfer between two concentric vertical cylinders, Numer. Heat Transfer A 53 (2008) 870–889.

[29] T. Basak, S. Roy, S.K. Babu, I. Pop, Finite element simulations of natural convection flow in an isosceles triangular enclosure filled with a porous medium: Effects of various thermal boundary conditions, Int. J. Heat Mass Transfer 51 (2008) 2733–2741.

[30] K. Khanafer, A. Al-Amiri, I. Pop, Numerical analysis of natural convection heat transfer in a horizontal annulus partially filled with a fluid-saturated porous substrate, Int. J. Heat Mass Transfer 51 (2008) 1613–1627.

[31] P. Bera, V. Eswaran, P. Singh, Numerical study of heat and mass transfer in an anisotropic porous enclosure due to constant heating and cooling, Numer. Heat Transfer A 34 (1998) 887–905.

[32] K. Slimi, L. Zili-Ghedira, S. Ben Nasrallah, A.A. Mohamad, A transient study of coupled natural convection and radiation in a porous vertical channel using the finite-volume method, Numer. Heat Transfer A 45 (2004) 451–478.

[33] F. Marcondes, J.M. de Medeiros, J.M. Gurgel, Numerical analysis of natural convection in cavities with variable porosity, Numer. Heat Transfer A 40 (2001) 403–420.

[34] Y. Varol, H.F. Oztop, I. Pop, Numerical analysis of natural convection in an inclined trapezoidal enclosure filled with a porous medium, Int. J. Therm. Sci. 47 (2008) 1316–1331.

[35] M. Peric, Natural-convection in trapezoidal cavities, Numer. Heat Transfer A 24 (1993) 213–219.

[36] R.A. Kuyper, C.J. Hoogendoorn, Laminar natural-convection flow in trapezoidal enclosures, Numer. Heat Transfer A 28 (1995) 55–67.

[37] M. Boussaid, A. Djerrada, M. Bouhadef, Thermosolutal transfer within trapezoidal cavity, Numer. Heat Transfer A 43 (2003) 431–448.

[38] A.C. Baytas, I. Pop, Natural convection in a trapezoidal enclosure filled with a porous medium, Int. J. Eng. Sci. 39 (2001) 125–134.

[39] J.N. Reddy, An Introduction to the Finite Element Method, McGraw-Hill, New York, 1993.

[40] T.J. Chung, Computational Fluid Dynamics, Cambridge University Press, London, 2002.

[41] Z.G. Du, E. Bilgen, Natural convection in vertical cavities with internal heat generating porous medium, Warme. Stoffubertrag 27 (1992) 149–155.
[42] G.K. Batchelor, An Introduction to Fluid Dynamics, Cambridge University Press, Cambridge, 1993.
[43] E. Natarajan, T. Basak, S. Roy, Natural convection flow in a trapezoidal enclosure with uniform and non-uniform heating of bottom wall, Int. J. Heat Mass Transfer 51 (2008) 747–756.
[44] M.M. Ganzarolli, L.F. Milanez, Natural-convection in rectangular enclosures heated from below and symmetrically cooled from the sides, Int. J. Heat Mass Transfer 38 (1995) 1063–1073.
[45] M. Hortmann, M. Peric, G. Scheuerer, Finite volume multigrid prediction of laminar natural-convection – bench-mark solutions, Int. J. Numer. Methods Fluids 11 (1990) 189–207.